Available online at www.sciencedirect.com
SCIENCE DIRECT®
Journal of Magnetic Resonance 170 (2004) 1–7
JMR Journal of Magnetic Resonance
www.elsevier.com/locate/jmr

SQUID detected NMR in microtesla magnetic fields

Andrei N. Matlachov, Petr L. Volegov, Michelle A. Espy,* John S. George, and Robert H. Kraus Jr.

Los Alamos National Laboratory, Biophysics Group, MS D454, Los Alamos, NM87545, USA

Received 23 December 2003; revised 20 May 2004
Available online 19 June 2004

Abstract

We have built an NMR system that employs a superconducting quantum interference device (SQUID) detector and operates in measurement fields of 2–25 μT. The system uses a pre-polarizing field from 4 to 30 mT generated by simple room-temperature wire-wound coils that are turned off during measurements. The instrument has an open geometry with samples located outside the cryostat at room-temperature. This removes constraints on sample size and allows us to obtain signals from living tissue. We have obtained ^{1}H NMR spectra from a variety of samples including water, mineral oil, and a live frog. We also acquired gradient encoded free induction decay (FID) data from a water-plastic phantom in the μT regime, from which simple projection images were reconstructed. NMR signals from samples inside metallic containers have also been acquired. This is possible because the penetration skin depth is much greater at the low operating frequencies of this system than for conventional systems. Advantages to ultra-low field NMR measurements include lower susceptibility artifacts caused by high strength polarizing and measurement fields, and negligible line width broadening due to measurement field inhomogeneity, reducing the burden of producing highly homogeneous fields.

1. Introduction

A primary thrust in clinical nuclear magnetic resonance (NMR) spectroscopy and magnetic resonance imaging (MRI) has been towards ever-higher magnetic field strengths. This is largely motivated by the enhanced sensitivity at high fields due to increased polarization and increasing detection efficiency at higher frequencies. Nevertheless, very-low field (VLF, in the mT range) and ultra-low field (ULF, in the μT range) NMR and MRI are areas of active interest motivated by a variety of reasons. Cost and size of systems could be significantly reduced [1]. VLF and ULF systems could be easily portable and the sample need not be restricted to the interior of a magnet bore (ex situ or ''inside out'' imaging). Low-field methods even enable imaging using the earth's magnetic field, ~50 μT [2], for a variety of applications including geophysical NMR measurements to characterize subsurface water, hydrocarbon deposits, or pollutant plumes [3–7].

NMR spectroscopy detects the magnetic signature of nuclear spins precessing in the measurement magnetic field at the characteristic Larmor frequency, ω_L. In a conventional system this signature is measured by Faraday detection in wire coils in a resonant circuit, where the induced voltage signal scales with ω_L. Thus at low fields (and correspondingly low ω_L) signals become increasingly difficult to measure with conventional detectors. The superconducting quantum interference device (SQUID) is a magnetic flux-to-voltage converter of exquisite sensitivity with a response that is independent of frequency. For this reason, a number of low-field NMR systems have employed SQUID sensors at measurement fields below 10 mT, (e.g., [8–17]) using both high-Tc (liquid nitrogen cooled) and low-Tc (liquid helium cooled) SQUIDs. Low-Tc SQUIDs provide higher sensitivity (due primarily to lower thermal noise) and greater reliability and robustness than presently available in high-Tc devices.

Measurement fields do not have to be highly homogeneous to achieve narrow NMR line widths at ULF. Moreover for a fixed relative homogeneity the NMR line width scales linearly with the strength of the

* Corresponding author. Fax: 1-505-665-4507.
E-mail address: espy@lanl.gov (M.A. Espy).

1090-7807/$ - see front matter © 2004 Elsevier Inc. All rights reserved.
doi:10.1016/j.jmr.2004.05.015

measurement field allowing the possibility of very narrow NMR lines with high signal-to-noise at ULF [11]. Susceptibility artifacts caused by coupling between the applied magnetic field and different sample materials broaden resonance lines at high fields but are significantly reduced at ULF. The absence of such artifacts may provide opportunities for novel forms of functional imaging at ULF. For example, we recently demonstrated the feasibility of magnetic resonance measurements with simultaneous magnetoencephalography (MEG), using the same detectors [18]. In addition, it may be possible to manipulate T_1 contrast at low field strength to provide significant contrast not realized at high fields. All of these effects combine to offer the possibility that NMR at low fields may provide a regime of high sensitivity and resolution, with unique applications.

2. Experimental set-up

A schematic diagram and details of the experimental set-up are shown in Fig. 1. The system used a low-Tc SQUID coupled to a superconducting second-order axial gradiometer as the detector. This detector is a typical design used in biomagnetic measurements [19]. The sample was pre-polarized in a magnetic field, B_p of 4–30 mT [1,11], while the measurement field, B_m, was ~3 orders of magnitude lower, between 2 and 25 μT. Operation at less than the earth's magnetic field was achieved by use of passive magnetic shielding [20] and by adjusting the measurement field to offset residual environmental fields. Passive shielding allows a wide range of measuring fields (and thus frequencies) from above to below the earth's magnetic field, and reduces the ambient magnetic noise detected by the SQUID sensors. B_p was generated by two coils positioned co-axial to the gradiometer and positioned such that the superposition of the fields from the two coils minimized the pre-polarization field coupling to the gradiometer. B_m was generated orthogonal to B_p by a square Helmholtz coil set. Gradient fields were generated along the direction of B_m by unbalancing the Helmholtz coils when measurements requiring a gradient were performed. It should be noted that we also were able to obtain free induction decays (FIDs) with the pre-polarizing field located perpendicular to both the gradiometer's axis and measurement field.

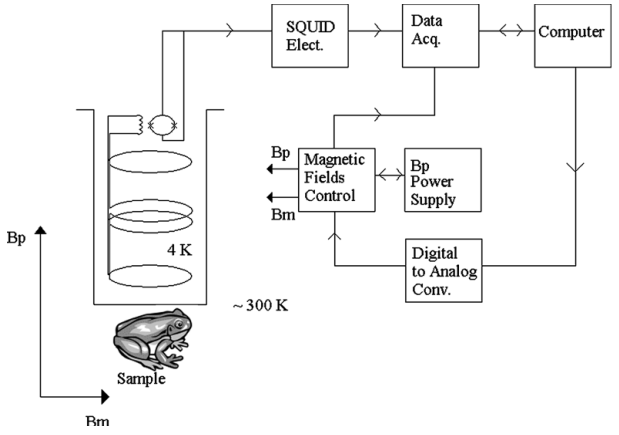

Fig. 1. Schematic diagram of the system developed for room-temperature μT NMR. The dewar is a fiberglass liquid helium SHE BMD-5 model. The system uses a low-Tc SQUID with 2 $\mu\Phi_0/\sqrt{\text{Hz}}$ noise connected to an axial superconducting second-order gradiometer. Gradiometer diameter is 14 mm and baseline is 50 mm. The pre-polarizing field, B_p, is provided by two 80 mm diameter coils, separated by ~60 mm, with 250 turns each. The coils are positioned around the tail of the cryostat co-axial to the gradiometer and adjusted to minimize pick-up. A square Helmholtz coil of length 56 cm provides the measurement field, B_m, orthogonal to B_p.

Samples were pre-polarized in B_p for a time greater than T_1 while the SQUID electronics were effectively turned off. The measurement field B_m was present continuously. At time $t = 0$, B_p was switched off in 0.5 ms, after which the SQUID electronics were activated, and the precession signal about B_m was measured. A dead time associated with SQUID recovery and dewar magnetization, the latter depending on the magnitude of B_p, was observed to be ~2 ms; small compared to T_1 and T_2 times for the samples. The spin precession signals were directly digitized at these low frequencies (100–1000 Hz) making heterodyne detection unnecessary.

The signal-to-noise (SNR) measured for a water sample at 10 mT B_p and 10 μT B_m was ~1 in a 100 Hz bandwidth and was enhanced through averaging. Another important strategy for SNR improvement is through the use of higher B_p fields. A factor of 10–20 enhancement should be straightforward for some applications.

3. Results

Free induction decay signals and spectra for the ^{1}H signal were obtained from a number of samples at ω_L from 90 to 1000 Hz. We consistently observed a difference in the apparent T_1 relaxation rate as a function of the magnitude of B_m. While a systematic investigation of the T_1 dependence on B_m must be completed, similar observations have been previously reported (e.g., [21]) suggesting the possibility of T_1 contrast imaging, for example by optimizing B_p and B_m.

Fig. 2 shows the FIDs and spectra for the ^{1}H signal from water and a live frog taken at ~10 μT. As indicated in Fig. 1, our samples are in the open, ~1 cm from the sensor coils. We present epoch-averaged data, however signals were visible in a 10 Hz bandwidth (SNR>1) even for a single epoch. The T_1 measured for the frog was 600 ms at 20 mT pre-polarization field.

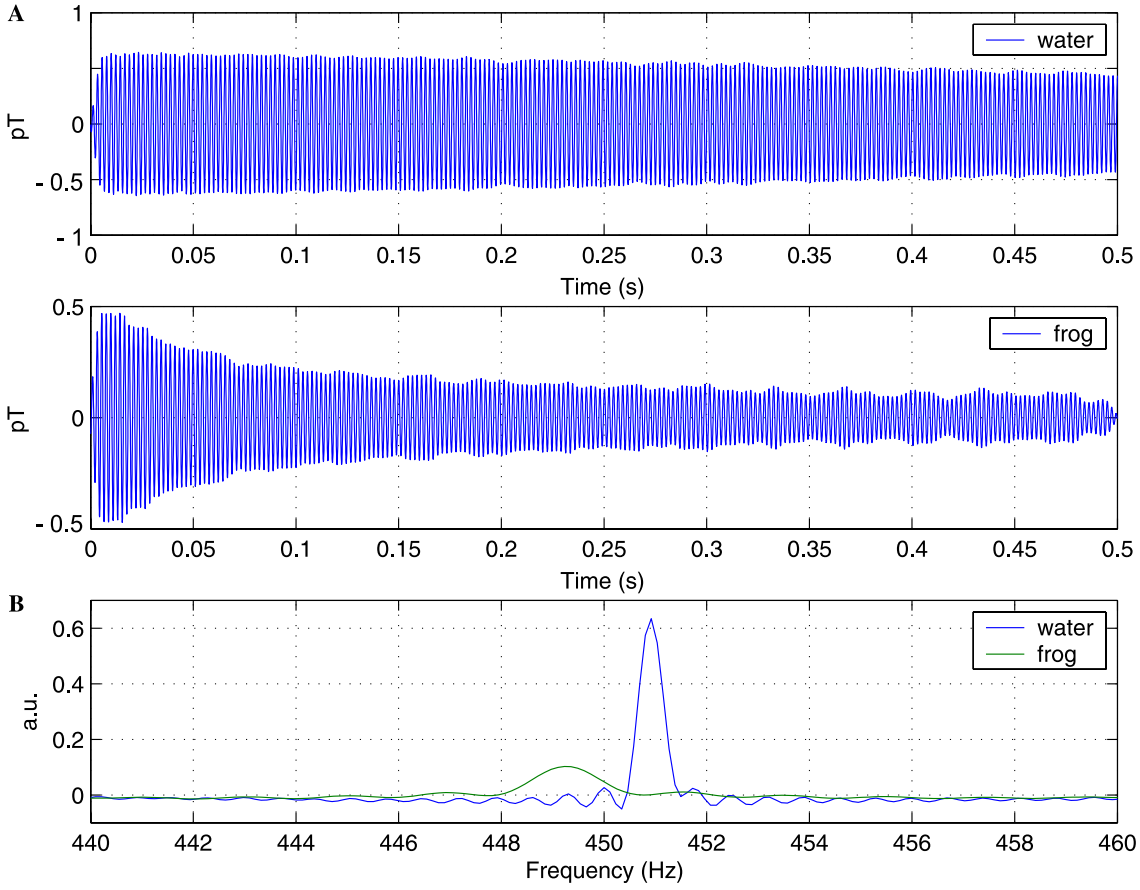

Fig. 2. (A) FIDs and (B) spectra for the ^{1}H signal from water and a live frog with $B_p = 20$ mT and $B_m \cong 10$ μT. The average over ~100 epochs is shown.

At the high frequencies characteristic of conventional high field MR imaging, neither the applied RF field nor the NMR signal produced by the sample can penetrate even a thin conductive shell because of the small skin depth. For example, at a 1 T field (proton $\omega_L = 42.6$ MHz) the penetration skin depth for copper is 10 μm, as compared to 10 mm at 1 μT ($\omega_L = 42.6$ Hz). This effect limits the utility of magnetic resonance of samples in metallic shells. The constraint is relaxed by performing NMR at ULF. Fig. 3 shows the FID and spectra for water taken inside a 2 mm thick copper canister at ~2 μT ($\omega_L = 87.9$ Hz). An example of the utility of such measurements is to food science, where conventional high field NMR has already become a powerful tool for the detection of moisture content, sugar content, adulteration, bacterial spoilage, etc. (see e.g., [22]). Our methods suggest a strategy for inspecting food inside metallic cans. We measured the ^{1}H NMR signal from tomato juice and cola inside unopened aluminum cans and observed very different T_2^* times: cola ~1500 ms, tomato juice ~300 ms.

Fig. 4 shows the one-dimensional gradient encoded frequency spectrum obtained from a simple water-plastic phantom. The phantom consisted of a plastic cylinder with six 4 mm diameter wells arranged in a row along the diameter (center to center distance 8 mm). All six filled holes are clearly resolved. The change in amplitude for the peaks representing the wells reflects a positional sensitivity that agrees well with our simulations. For these measurements $B_m = 7.8$ μT and the gradient was 8 μT/m. Fig. 5A is a photograph of a 60 mm diameter by 52 mm high cylindrical plastic phantom with seven 10 mm diameter by 48 mm deep wells. Four of the wells were filled with water (shown filled with colored water for visibility). Fig. 5B illustrates a 2D image of the phantom constructed from a series of gradient encoded FID spectra acquired at various angles by rotating the sample within a fixed measurement field. The measurement field was 7.8 μT and the gradient was ~7 μT/m. Given the small B_m field, we note that it would also be easy to rotate the field and gradient orientation to arbitrary directions using a fixed set of field coils and appropriately phasing the relative current amplitudes.

4. Discussion

Imaging at fields of 1–10 mT has previously been demonstrated [10,13,14,16] and has been reported

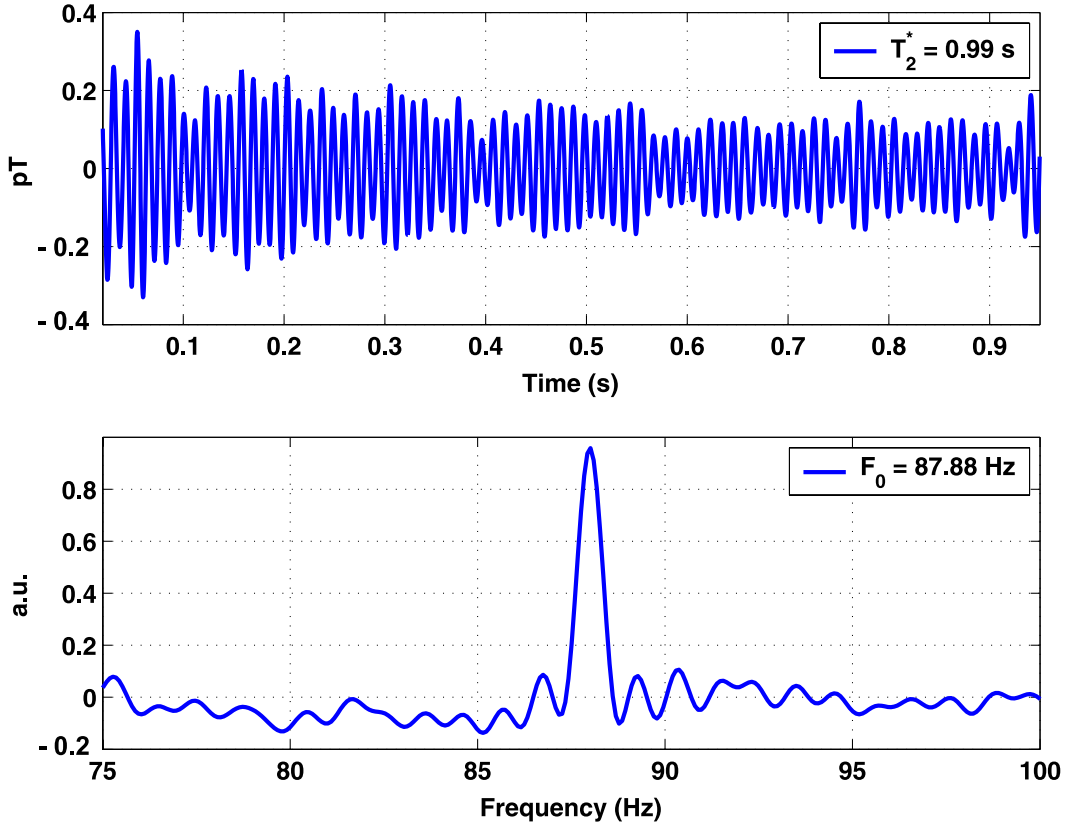

Fig. 3. FID and spectra for water taken inside a 2 mm thick copper canister at $B_p = 10$ mT and $B_m \sim 2$ μT (Larmor frequency 87.9 Hz). The average over ~100 epochs is shown.

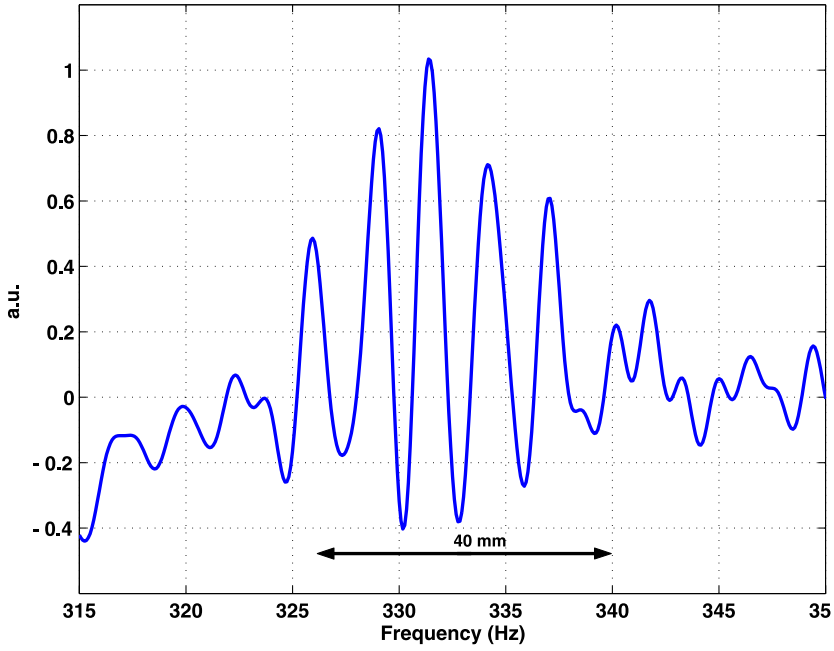

Fig. 4. Gradient encoded NMR spectra for a water phantom consisting of a plastic cylinder with six 4 mm diameter wells arranged in a row along the diameter (center to center distance 8 mm). $B_p = 10$ mT and $B_m = 7.8$ μT. The gradient was 8 μT /m. The average over ~200 epochs is shown.

at 130 μT [23]. To our knowledge, the phantom results we present in this paper are the first MR images in the 10 μT regime with a sample outside of the cryostat. By working at ULF, we achieved narrow line widths that approach the natural line width.

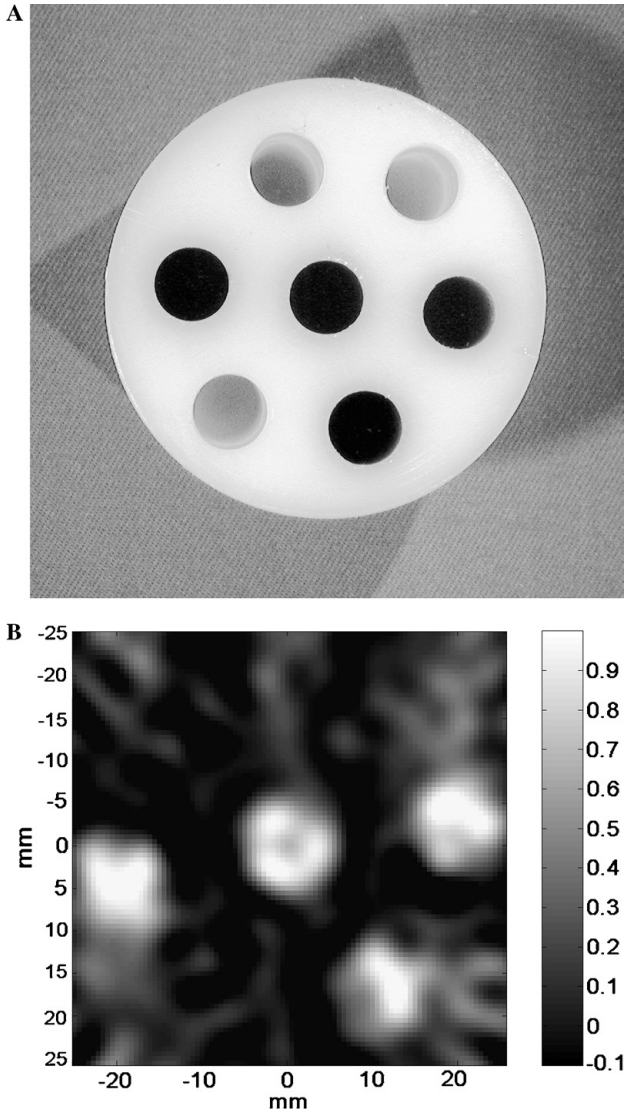

Fig. 5. (A) Photograph of a 60 mm diameter cylindrical plastic phantom with seven 10 mm diameter wells. Four of the wells were filled with water (pictured filled with colored water for visibility). (B) 2D image of the phantom constructed from a series of gradient encoded FID spectra acquired by rotating the sample within a fixed measurement field. $B_p = 17\,\text{mT}$, B_m was 7.8 μT and the gradient was ~7 μT/m. The gradient was produced by slightly unbalancing the current in the Helmholtz coils producing B_m. The average over ~100 epochs is shown.

A principal objective of this work was to demonstrate the feasibility of NMR and MRI at ULF, a regime that ultimately may have numerous applications. One such application is simultaneous MRI and MEG measurements, two techniques previously considered incompatible. Simultaneous MEG and ULF MRI may alleviate some of the difficulties imposed by the current need to co-register separately acquired MEG and high field MRI data [24]. We recently demonstrated simultaneous ULF NMR and MEG [18]. Simultaneous MRI and MEG will require imaging at the lowest fields possible to minimize interference with MEG signal acquisition. In addition, concurrent biomagnetic measurements and dynamic anatomical imaging might have important advantages for applications such as diagnostic cardiac imaging.

While spectroscopy based on chemical shift, which scales with field strength, is unlikely to be observable at ULF, other spectral phenomena such as *J*-coupling are independent of field strength and can be observed with significant SNR [11]. Finally, other forms of "spectroscopy" such as nuclear identification based on the gyromagnetic ratio will be greatly facilitated by the broadband sensitivity of SQUIDs coupled with the nonspecific excitation provided by DC pre-polarization and field cycling (eliminating the need for tuned RF pulse and detection coils).

Because B_m orientation is arbitrary (i.e., it is not fixed by the large static field of the imaging magnet), gradient design is simplified i.e., all gradients can employ designs analogous to the *z*-axis gradient of a conventional imager. The flexibility of choosing B_p and B_m orientations may enable the design of gradient fields to minimize parasitic gradients. Parasitic gradients will be further reduced by the smaller gradient requirements for imaging that allow larger coils, placed further from the imaging volume, to achieve the required gradient strengths.

Imaging of dynamic physiological processes and in particular functional imaging of neural activity drives a requirement for much faster imaging. While MRI at ULF has numerous advantages, a variety of new challenges are presented. The narrow line widths of ULF measurements may allow us to improve imaging resolution without a corresponding increase in gradient strength. Preliminary data indicates that for some relevant biological matter [23,25] at ULF $T_1 \approx T_2$. In these instances the delay between successive acquisitions may be reduced. Imaging at ULF with lower field gradients will require tighter frequency resolution than for conventional high field imaging. This, through the Nyquist theorem, limits the minimum acquisition time. Moreover, in this regime natural line width becomes a factor in limiting spatial resolution. A number of labs have explored the use of phased arrays for detection coupled with novel image reconstruction techniques [26,27]. We plan to apply an existing dense-array SQUID sensor system designed for MEG applications [28] to study alternative approaches to increase MR imaging speed at ULF.

Another intriguing potential application of ULF MRI would be direct imaging of the physiological currents from muscle, heart, and brain [29,30]. This method of directly imaging neuronal activity would not have the inherent ambiguity associated with the inverse problem of electromagnetic source localization from field measurements on a surface. In principle, measurement of frequency, phase, and/or T_2^* effects at ULF might be used to detect perturbations of local magnetic field due to physiological currents. For neural currents in the brain, typical sensory evoked responses measured at the surface with

SQUIDs are in the range of 50–500 fT, while the largest spontaneous responses associated with endogenous rhythms such as alpha, or with epileptic activity are on the order of 10 pT at the head surface e.g., [19]. Accounting for the separation between source and sensors and assuming a dipole source, one can estimate the neural magnetic field in situ to be in the range of 100 pT to 1 nT. This is 3–5 orders of magnitude smaller than the measurement fields used here, and 9–11 orders smaller than typical MR imaging techniques. Signal-to-noise limitation will be a significant challenge in such measurements but can be addressed by signal averaging and other strategies for signal-to-noise optimization. Moreover, measurements at ULF will greatly reduce the contribution of physiological noise from cardiac and respiratory cycles due to the paramagnetic nature of deoxyhemoglobin.

5. Conclusions

NMR/MRI at low fields introduces a host of new applications including true ex situ imaging, ''pure J spectroscopy'' [11], and low-cost MR instrumentation [1,13]. With the reduction in susceptibility noise and enhanced resolution at low fields, it is now possible to conduct simultaneous NMR/MRI and MEG or other biomagnetic measurements [18]. It may also be possible to use this method for direct imaging of the magnetic fields due to neural currents. Our work has demonstrated basic proton spectroscopy at microtesla fields, and extended the measurements to simple imaging with samples located outside of the cryostat, demonstrating that there are no fundamental limitations to prevent anatomical or functional imaging of a human subject. NMR inside metal containers has also been demonstrated, something that could not be accomplished with conventional high-field methods.

Acknowledgments

The authors wish to thank Dr. C.C. Wood for his thoughtful discussions of the topics presented. Technical development of the instrumentation used for this work was supported by Los Alamos National Laboratory and DARPA. Experimental studies received support from the US Department of Energy, Office of Biological and Environmental Research. Care and use of animals was consistent with protocols approved by the Los Alamos IACUC.

References

[1] A. Macovski, S. Conolly, Novel approaches to low cost MRI, Magn. Reson. Med. 30 (1993) 221–230.
[2] J. Stepišnic, V. Eržen, M. Kos, NMR imaging in the Earth's magnetic field, Magn. Reson. Med. 15 (1990) 386–391.
[3] G.J. Bene, Nuclear magnetism of liquid systems in the Earth field range, Phys. Rep. 58 (4) (1980) 213–267.
[4] G.J. Bene, Spin echoes in zero mean field, Comptes Rendus Hebdomadaires des Seances de l'Academie des Sciences, Serie B (Sciences Physiques) 271 (25) (1970) 1235–1237.
[5] R.K. Cooper, J.A. Jackson, Remote (inside-out) NMR.I. Remote production of a region of homogeneous magnetic field, J. Magn. Reson. 41 (3) (1980) 400–405.
[6] L.J. Burnett, J.A. Jackson, Remote (inside-out) NMR. II. Sensitivity of NMR detection for external samples, J. Magn. Reson. 41 (3) (1980) 406–410.
[7] J.A. Jackson, L.J. Burnett, J.F. Harmon, Remote (inside-out) NMR. III. Detection of nuclear magnetic resonance in a remotely produced region of homogeneous magnetic field, J. Magn. Reson. 41 (3) (1980) 411–421.
[8] N.Q. Fan, M.B. Heaney, J. Clarke, D. Newitt, L.L. Wald, E.L. Hahn, A. Bielecki, A. Pines, Nuclear magnetic resonance with DC SQUID preamplifiers, IEEE Trans. Magn. 25 (2) (1989) 1193–1199.
[9] M.P. Augustine, D.M. TonThat, J. Clarke, SQUID detected NMR and NQR, Solid State Nucl. Mag. Res. 11 (1998) 139–156.
[10] K. Schlenga, R.F. McDermott, J. Clarke, R.E. de Souza, A. Wong-Foy, A. Pines, Low-field magnetic resonance imaging with a High-Tc dc superconducting quantum interference device, Appl. Phys. Lett. 75 (23) (1999) 3695–3697.
[11] R. McDermott, A.H. Trabesinger, M. Mück, E.L. Hahn, A. Pines, J. Clarke, Liquid-state NMR and scalar couplings in microtesla magnetic fields, Science 295 (2002) 2247–2249.
[12] H.C. Seton, D.M. Bussell, J.M.S. Hutchison, I. Nicholson, D.J. Lurie, DC SQUID-based NMR detection from room temperature samples, Phys. Med. Biol. 37 (11) (1992) 2133–2138.
[13] H.C. Seton, J.M.S. Hutchison, D.M. Busell, A 4.2K receiver coil and SQUID amplifier used to improve SNR of low-field magnetic resonance images of the human arm, Meas. Sci. Technol. 8 (1997) 198–207.
[14] H.C. Seton, J.M.S. Hutchison, D.M. Bussell, A tuned SQUID amplifier for MRI based on a DOIT flux locked loop, IEEE Trans. Appl. Supercond. 7 (2) (1997) 3213–3216.
[15] S. Kumar, B.D. Thorson, W.F. Avrin, Broadband SQUID NMR with room-temperature samples, J. Magn. Reson. B 107 (1995) 252–259.
[16] S. Kumar, W.F. Avrin, B.R. Whitecotton, NMR of room temperature samples with a flux-locked dc SQUID, IEEE Trans. Magn. 32 (6) (1996) 5261–5264.
[17] S. Kumar, R. Mathews, S.G. Haupt, D.K. Lathrop, M. Takigawa, J.R. Rozen, S.L. Brown, R.H. Koch, Nuclear magnetic resonance using a high temperature superconducting quantum interference device, Appl. Phys. Lett. 70 (8) (1997) 1037–1039.
[18] P. Volegov, et al., Simultaneous magnetoencephalography and SQUID detected nuclear magnetic resonance in microtesla magnetic fields, Magn. Reson. Med., in press.
[19] M. Hämäläinen, R. Hari, R.J. Ilmoniemi, J. Knuutila, O.V. Lounasmaa, Magnetoencephalography-theory, instrumentation, and applications to noninvasive studies of the working human brain, Rev. Mod. Phys. 65 (2) (1993) 413–497.
[20] G. Sullivan, P. Lewis, J.S. George, E.R. Flynn, A magnetic shielded room designed for magneto-encephalography, Rev. Sci. Instrum. 60 (4) (1989) 765–770.
[21] U.A. Ramadan, A.T. Markkola, J. Halavaara, J. Tanitu, A.M. Hakkinen, H.J. Aronen, On- and off resonance spin-lock MT imaging of normal human brain at 0.1T: possibilities to modify image contrast, Magn. Reson. Imaging 16 (10) (1998) 1191–1199.
[22] I.L. Pykett, NMR—a powerful tool for industrial process control and quality assurance, IEEE Trans. Appl. Superconduct. 10 (1) (2000) 721–723.

[23] S-K. Lee, M. Moessle, W. Myers, N. Kelso, R. McDermott, A. Trabesinger, A. Pines, J. Clarke, MRI in microtesla fields detected by a superconducting quantum interference device (SQUID), presented at the 45th Experimental Nuclear Magnetic Resonance Conference, April 18–23, 2004, Asilomar Conference Center, Pacific Grove, CA.

[24] J.S. George, C.J. Aine, J.C. Mosher, D.M. Ranken, H.A. Schlitt, C.C. Wood, J.D. Lewine, J.A. Sanders, J.W. Belliveau, Mapping function in the human brain with MEG, anatomical MRI, and functional MRI, J. Clin. Neurophysiol. 12 (5) (1995) 406–431.

[25] H.W. Fischer, P.A. Rinck, Y. Van Heverbeke, R.N. Muller, Nuclear relaxation of human brain gray and white matter: analysis of field dependence and implications for MRI, Magn. Reson. Med. 16 (1990) 317–334.

[26] D.K. Sodickson, W.J. Manning, Simultaneous acquisition of spatial harmonics (SMASH): fast imaging with radiofrequency coil arrays, Magn. Reson. Med. 38 (4) (1997) 591–603.

[27] K.P. Pruessmann, M. Weiger, M.B. Scheidegger, P. Boesiger, SENSE: sensitivity encoding for fast MRI, Magn. Reson. Med. 42 (5) (1999) 952–962.

[28] R.H. Kraus Jr., P. Volegov, K. Maharajh, A. Matlachov, M. Espy, E.R. Flynn, Source localization using a novel SQUID-based superconducting imaging-surface system, Physica C 368 (2002) 18–23.

[29] J. Bodurka, P.A. Bandettini, Toward direct mapping of neuronal activity: MRI detection of ultra-weak, transient magnetic field changes, Magn. Reson. Med. 47 (2002) 1052–1058.

[30] J.H. Xiong, P.T. Fox, J.H. Gao, Directly mapping magnetic field effects of neuronal activity by magnetic resonance imaging, Hum. Brain Mapp. 20 (2003) 41–49.